Interpretation of the early stiffening process in alkali-activated slag pastes

Sun, Yubo; de Lima, Luiz Miranda; Rossi, Laura; Jiao, Dengwu; Li, Zhenming; Ye, Guang; De Schutter, Geert

DOI
10.1016/j.cemconres.2023.107118

Publication date
2023

Document Version
Final published version

Published in
Cement and Concrete Research

Citation (APA)
Sun, Y., de Lima, L. M., Rossi, L., Jiao, D., Li, Z., Ye, G., & De Schutter, G. (2023). Interpretation of the early stiffening process in alkali-activated slag pastes. *Cement and Concrete Research*, *167*, Article 107118. https://doi.org/10.1016/j.cemconres.2023.107118

Cement and Concrete Research 167 (2023) 107118

Contents lists available at ScienceDirect

Cement and Concrete Research

journal homepage: www.elsevier.com/locate/cemconres

Interpretation of the early stiffening process in alkali-activated slag pastes

Yubo Sun [a], Luiz Miranda de Lima [b], Laura Rossi [c,d], Dengwu Jiao [a], Zhenming Li [b], Guang Ye [a,b], Geert De Schutter [a,*]

[a] Magnel-Vandepitte Laboratory, Department of Structural Engineering and Building Materials, Ghent University, 9052 Ghent, Belgium
[b] Microlab, Section of Materials and Environment, Faculty of Civil Engineering and Geosciences, Delft University of Technology, Stevinweg 1, 2628 CN Delft, the Netherlands
[c] Institute of Building Materials and Concrete Structures (IMB), Karlsruhe Institute of Technology (KIT), DE-76131 Karlsruhe, Germany
[d] Materials Testing and Research Institute Karlsruhe (MPA), Karlsruhe Institute of Technology (KIT), DE-76131 Karlsruhe, Germany

ARTICLE INFO

Keywords:
Alkali-activated slag
Early stiffening
Microstructure
Rheology
Reaction products

ABSTRACT

To better understand early stiffening of AAS pastes, distinctive microstructural features by varying the silicate modulus (Ms) have been visualized with in-situ microscopy. In addition, the activation reaction was monitored with multiple approaches, while solid and liquid phases in hydrating AAS were characterized separately. In silicate-activated AAS, it was found fine granules of reaction products are intensively dispersed in the activator solution, leading to a less flocculated system. Compared to hydroxide-activated AAS, the development of interparticle connections was limited at early ages, whereas reaction products were detected with much smaller grain size, less crystalline phase, and higher Al incorporation. Results indicate that the stiffening of hydroxide-activated AAS is attributed to the formation of a well-percolated network through solid reaction products. Instead, massive fine granules of reaction products dispersed in the pore solution continuously develop, which may intensify the interparticle interactions and macroscopically results in the stiffening of a silicate-activated AAS.

1. Introduction

In view of the heavy emission and energy consumption, global climate change associated with the vast Portland cement (PC) production has become a major concern worldwide. Alternative binders have been widely discussed and studied in recent years, aiming to reduce the carbon footprint of construction materials [1,2].

By making use of various industrial waste and by-products as precursors, alkali-activated material (AAM) is developed as a green binder, which saves CO_2 emissions from the calcination of cement clinkers [3]. However, the application of highly concentrated alkaline activators might on the other hand rise the environmental impact, especially the sodium silicate, which is produced from high energy-consuming processes [4]. It has been suggested that the application of AAMs reduces 9–80 % CO_2 compared to PC binders [5]. The activation reaction takes place in alkaline media, where the aluminosilicate precursors are dissolved and reassembled into ordered crosslinking structures through polymerization reactions [3,6,7]. It has been reported that AAMs may provide equivalent mechanical properties and superior chemical resistance compared to PC materials [8–10].

Nevertheless, a critical issue appears as the rapid workability loss of alkali-activated slag (AAS) mixtures, in particular with the presence of silicate in activators [11]. Limited setting time and uncontrolled stiffening process have been frequently reported in silicate-activated AAS [12–14], leading to great challenges in the mixing, delivery, pumping, casting, and consolidation of fresh mixtures. Previous studies have illustrated the significant influence of silicate modulus (Ms) on the mineralogical and chemical properties of reaction products in AAS [15,16]. It has been suggested that the rapid setting is attributed to the accumulation of primary C-(A)-S-H gels [11,17,18]. However, the characterization is challenging due to complex reactions and the amorphous nature of reaction products, whereas a clear description of such primary reaction products is still absent to date. Moreover, previous investigations have separated the pore solution and solid particles for characterization. It remains uncertain how they would contribute to the stiffening of AAS mixtures from the spatial configuration point of view. As a consequence, microstructural features of liquid and solid phases in fresh mixtures are not properly considered, which should have

* Corresponding author.
E-mail address: geert.deschutter@ugent.be (G. De Schutter).

https://doi.org/10.1016/j.cemconres.2023.107118
Received 10 November 2022; Received in revised form 1 February 2023; Accepted 9 February 2023
Available online 2 March 2023

played a significant role to affect the fresh properties. A few recent literature have reported distinctive rheological behaviors in mixtures prepared with sodium silicate activators compared to PC materials [19–21]. It is indicated the solid-liquid interactions become rather complex due to the inclusion of alkaline substances in the activator solution. It appears that the current knowledge of PC materials is insufficient to explain the structural build-up and rheology evolution in AAS.

A previous paper has illustrated the effect of activators on the microstructural configuration in fresh AAS pastes by using the cryo-SEM technique [16]. In the current study, a comprehensive investigation was conducted to further explore the microstructure evolution along the early stiffening process in AAS. In-situ microscopy was first conducted to assess the evolution of microstructural features in different alkaline media. Vicat needle penetration, calorimetry, ultrasonic pulse velocity (UPV), and small amplitude oscillation shear (SAOS) tests were performed to interpret the physical parameter variations along the early stiffening process. Meanwhile, pore solution and solid reaction products were characterized as a function of time to evaluate the phase evolution in hydrating AAS. Finally, separate models have been proposed, which schematically illustrate the early stiffening process of hydroxide- and silicate-activated AAS pastes.

2. Experimental method

2.1. Materials

In this study, ground granulated blast furnace slag (BFS) was used as the precursor to prepare AAS mixtures, which was provided by Ecocem Benelux B.V. Chemical compositions detected by X-ray fluorescence (XRF) spectroscopy and physical properties are summarized in Table 1. The particle size distribution of BFS measured by laser diffraction is presented in Fig. 1(a) (d_{50}=8.28 μm). The morphology of angular BFS particles with irregular shapes was observed by scanning electron microscope (SEM) as shown in Fig. 1(b).

Two kinds of alkaline compounds: sodium hydroxide and sodium silicate were used in this study to prepare the alkaline activator. Reagent-grade sodium hydroxide anhydrous pearls (>99 %) were provided by Brenntag N.V., and the sodium silicate solution (15 % Na_2O, 30 % SiO_2, and 55 % water) was provided by PQ Corporation.

2.2. Mixture proportions

Details of mix designs are listed in Table 2. The water to binder (w/b) ratio was kept at 0.4 among all mixtures to ensure adequate consistency, while the Na_2O concentration was fixed at 4 % in AAS pastes. It has been reported that the silicate modulus (Ms, indicating the molar ratio between SiO_2 and Na_2O) of the activator plays a decisive role in reaction kinetics of AAS [15]. By varying the Ms between 0 and 1, M1 to M4 were designed to evaluate the influence of silicate species in activators. Sodium hydroxide was used as the sole alkaline compound in M1, which represents the limiting case that no silicate was involved in the activator (Ms0). A relatively low Ms of 0.05 was applied in M2 to investigate the rapid growth in early-age ultrasonic pulse velocity (UPV) evolution when sodium silicate presents in the activator. M3 and M4 were designed with higher Ms of 0.5 and 1.0, respectively. The mixture proportions used in this study are expressed as per 100 g of precursor. Activators were prepared by dissolving sodium hydroxide and sodium silicate solution in tap water 24 h before mixing.

2.3. Testing program

2.3.1. In-situ microscopy on diluted systems

In-situ microscopy was first conducted with a Leica DMC 4500 optical microscope to assess the microstructure evolution of individual BFS particles along the activation process. Sodium hydroxide (3 mol/L) and sodium silicate (Ms = 1.0) solutions were prepared with an identical sodium concentration to simulate the alkaline condition in AAS mixtures for activation reactions. BFS was passed through a series of sieves and the fraction with a particle size between 40 and 63 μm was used for microscopy. It should be noticed that the current test is performed on diluted systems, where the liquid to solid ratio is significantly higher than concentrated AAS pastes to speed up the initial dissolution and subsequent reactions. However, the results should be representative of an ideal condition in the fresh mixture after mixing that each slag particle is surface saturated by the activator solution. The results are not in the same timeline as real AAS pastes. The features of microstructure evolution around individual slag particles will be further discussed to better understand the early-stiffening process in AAS.

For each test, as presented in Fig. 2, BFS particles were uniformly sprinkled on a glass slide [22]. A drop of activator was then added to initiate the activation reaction. Eventually, a coverslip was applied on the top of the glass slide to seal the liquid and solid particles for visualization. The microstructure evolution of BFS particles in different alkaline media was continuously recorded for 24 h under 200 × magnifications. The analysis was repeated on 10 individual BFS particles and the most representative is presented in this study.

2.3.2. Preparation of AAS pastes

The fresh AAS pastes used in this study were prepared with a Hobart planetary mixer by blending 500 g slag and corresponding activators shown in Table 2. The solid precursor was first dry-blended in the mixer for 60 s. Activator solutions were then gradually added into the mixer in 10 s. Each AAS paste was first mixed at low speed (140 ± 5 rpm) for 90 s, followed by a high-speed mixing at 285 ± 5 rpm for another 90 s. The mixing procedure takes 180 s since the wetting of precursors, and fresh AAS pastes obtained were used for subsequent tests described below.

2.3.3. Monitoring on the early-stage reaction process

In this study, the early stiffening process of AAS pastes was monitored by the following approaches.

The setting process of different mixtures was measured with an automatic Vicat needle apparatus according to EN 196-3. Fresh AAS pastes were loaded into a conical Vicat mold for the needle penetration test, which was conducted with an ambient condition at 20 ± 1 °C under 65 % relative humidity. The penetration depth of each measurement was recorded as a function of time until mixtures developed complete resistance against the needle penetration.

The exothermic behavior along the early-stage reactions was detected by a TAMAIR isothermal calorimeter. About 14 ± 0.01 g of the fresh paste after mixing was immediately loaded into a glass ampoule, which was subsequently sealed and transferred into isothermal channels of the calorimeter. Quartz sand with a specific heat flow of 0.71 J/(g·K) was applied as an inert reference. The heat flow was recorded as the difference between the sample and reference [23] at 20 ± 0.5 °C for 24 h. The

Table 1
Chemical composition (by mass percentage) and physical properties of BFS.

	CaO	SiO_2	Al_2O_3	MgO	SO_3	TiO_2	K_2O	Fe_2O_3	LOI[a]	Blaine area (m^2/kg)	Specific gravity
	(%)										
BFS	40.9	31.1	13.7	9.16	2.31	1.26	0.69	0.40	0.10	428	2.89

[a] Loss on Ignition (LOI) measured by TG analysis at 950 °C.

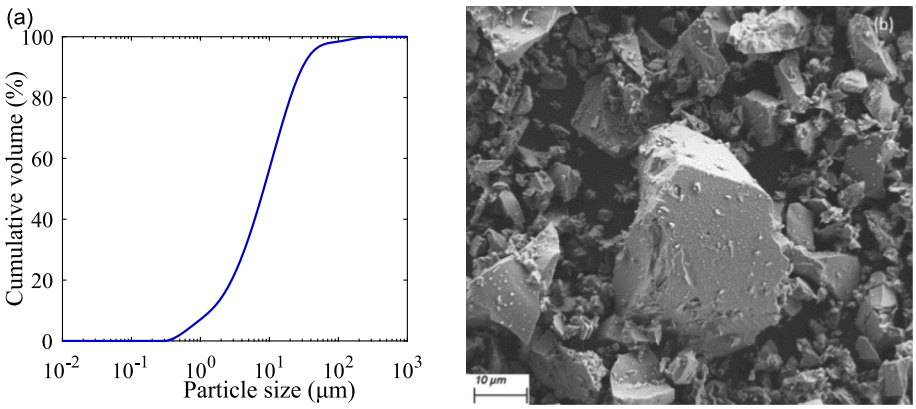

Fig. 1. Physical properties of BFS (a) particle size distribution; (b) morphology by SEM.

Table 2
Mixture proportions of AAS pastes.

Mix	BFS (g)[a]	Activator solution						w/b[e]
		Sodium hydroxide (g)	Sodium silicate (g)	Extra water (g)	Na_2O[b]	Ms[c]	pH[d]	
M1	100	5.16	0.00	42.06	4 %	0	13.78	0.4
M2	100	5.03	0.67	41.77	4 %	0.05	13.76	0.4
M3	100	3.87	6.67	39.08	4 %	0.5	13.64	0.4
M4	100	2.58	13.33	36.10	4 %	1	13.47	0.4

[a] The mass of precursor was fixed at 100 g for each mixture in this study.
[b] Represented as the mass percentage of BFS.
[c] Defined as the molar ratio between SiO_2 and Na_2O in activators.
[d] Determined by Extech PH150 pH-meter at 20 ± 0.5 °C.
[e] Defined as water content in both aqueous activator and water added separately from the activator divided by the sum of precursor and solid activators.

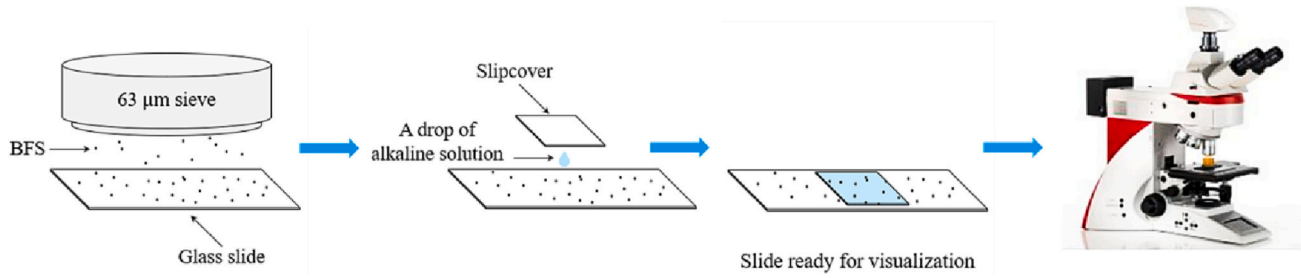

Fig. 2. Scheme for in-situ microscopy visualization.

results present in this study are normalized into 1 g of slag. Due to the thermal disturbance while inserting the glass ampoule, the heat recorded at the first 30 min was not compared among different samples.

Ultrasonic pulse velocity (UPV) of AAS paste was detected by the FreshCon system [24] for 24 h, and the test was conducted in an ambient chamber at 20 ± 1 °C and 65 % relative humidity. For each measurement, approximately 400 mL of AAS paste was loaded into a U-shaped container. A plastic foil was applied on the top of the container to prevent moisture evaporation during the measurement. The propagation speed of ultrasonic waves was recorded by the FreshCon system every 30 s to monitor the structural connectivity of the stiffening AAS paste.

In addition, the early-age structural build-up was also assessed by small amplitude oscillation shear (SAOS) tests with an Anton Paar MCR 102 rheometer (fitted with a 6-blade vane, 22 mm in diameter, and 16 mm in height), in both continuous and intermittent patterns [25]. The fresh AAS paste was loaded into a cylindrical cup (27.6 mm inner diameter and 75 mm depth), and the temperature was controlled at 20 ± 0.5 °C with a water-bath system. Before each measurement, the paste was subjected to a 30-s pre-shear at 100 s^{-1} to reach a reference state [20,21], and then left at rest to release the residual stress [26]. To ensure the structure of AAS paste is not destructed by the continuous excitation during SAOS tests, a strain sweep from 0.0001 % to 10 % was first conducted with a fixed frequency of 1 Hz to determine the linear viscoelastic domain (LVED) [20,25]. Subsequently, a time sweep was conducted at 1 Hz with a constant strain amplitude of 0.005 % (within the LVED) until 90 min. The intermittent SAOS test was parallelly performed on AAS paste to explore the evolution of stress-strain responses and structural build-up in each 10 min timeframe. In specific, a strain sweep (from 0.0001 % to 10 %, 1 Hz) was first conducted for 60 s at the beginning of each testing section, followed by a 9-min time sweep (0.005 %, 1 Hz). Such sequence was repeated every 10 min. Both the continuous and intermittent SAOS tests were started 10 min after the wetting of precursors until 90 min or the capacity of the rheometer was reached. The SAOS test was performed on 3 replicate samples to ensure repeatability, and the curve most close to the average is presented.

2.3.4. *Characterization of hydrating AAS pastes*

The pore solution and solid components in hydrating AAS pastes were characterized separately along the reaction process.

Chemical analysis was performed on the pore solution of AAS paste

every 10 min after the wetting of precursors until 90 min, and the '0-min' result denotes the composition of activator solutions. Fresh AAS pastes were loaded into plastic tubes and centrifuged at 3500 rpm for 6 min to separate the liquid phase [27]. Afterwards, the liquid phase on the top layer after centrifugation was extracted with a syringe to pass through a 45 μm polyethersulfone membrane filter. The chemistry of pore solutions was analyzed by Inductively Coupled Plasma - Optical Emission Spectrometry (ICP-OES) 720 ES Varian/Agilent to determine the concentration of Ca, Na, Al, Si, and Mg ions as a function of time (Note: Na and Si were diluted with pure water at 1:4000, while the rest elements were diluted at 1:20 for analysis).

Moreover, the bulk solid fraction including the unreacted precursor and reaction products in AAS pastes were characterized at different ages. Three target ages were defined as 30, 60, and 90 min, respectively. A solvent replacement treatment with water and isopropanol, as proposed by Palacios et al. [11], was applied to arrest the activation reaction. Solid residues collected from filtration with a 45 μm membrane were vacuum dried and further ground to pass a 63 μm sieve. The solid powder obtained was characterized by thermogravimetric analysis (TGA), X-ray diffraction (XRD), and Fourier transform infrared (FTIR) spectroscopy tests as follows:

- TGA was performed with a TG-449-F3-Jupiter instrument to assess the reaction products. Around 50 mg of solid powder was incinerated in an aluminum oxide crucible from 40 to 900 °C at 10 °C/min in argon atmospheres, and the mass evolution as a function of temperature was recorded.
- XRD tests were conducted using a Bruker D8 Advance diffractometer with Cu-Kα radiation (λ = 1.54 Å). XRD patterns were recorded at the range between 5° and 70° with a step size of 0.02°.
- FTIR spectra were detected with a Spectrum TM 100 Optical ATR-FTIR spectrometer from 600 to 1300 cm^{-1} with a resolution of 1 cm^{-1}.

3. Results and discussion

3.1. In-situ microscopy on diluted systems

The microstructure evolution of BFS particles in sodium hydroxide and sodium silicate solutions are presented in Figs. 3 and 4, respectively (more details can be found in Video 1 in Supplementary data). In both cases, the visual field has been focused on an individual BFS grain with a particle size of about 50 μm. An angular-shaped BFS particle was observed at 0 h, where a clear boundary could be identified on the grain surface. Besides, some fine BFS particles were found to attach to the big grain.

In hydroxide media, as shown in Fig. 3, nucleation of solid reaction products has been observed after 1 h. It can be seen that the majority of small solid particles were closely attached to the slag surface, whereas a few of them were distributed adjacent to the big slag grain. As the reaction proceeded, the particle size of the big slag grain gradually declined between 1 and 4 h. Meanwhile, growth in the particle size of solid reaction products has been observed along with the dissolution of BFS. Up to 6 h, the slag surface has been almost fully covered with a thick layer of reaction products. Ben Haha et al. [28] reported the fast precipitation of relatively dense hydrates around the slag particles by using NaOH activators, whereas further hydrates seldom developed in the empty interparticle pore space. Similarly, as shown in Fig. 3, it appears that further reactions were obstructed by the outer layer and the microstructural features did not significantly evolve in later ages.

On the other hand, a distinctive microstructure evolution process has been observed in the sodium silicate solution (Fig. 4). A continuous dissolution of slag particles has been detected that they nearly disappeared after 24 h. Compared to Fig. 3, the slag surface remained smooth at early ages. No obvious nucleation of solid reaction products has been observed on the slag surface up to 4 h. Instead, the liquid phase around the slag particle turned less transparent after 6 h. At 8 h, it can be observed that numerous fine granules have been nucleated, which were intensively dispersed in the liquid phase. Subsequently, the particle size of fine granules gradually increased as the reaction progressed. However, the solid reaction products formed in silicate media are much smaller than those formed in the sodium hydroxide solution. It is noteworthy that the solid grains dispersed in the liquid phase remained relatively separated from each other, and no apparent coagulation or flocculation has been observed in the system.

The structural build-up in PC materials is a combined result of physical interactions and chemical hydration [29]. After mixing, cement particles dispersed in the suspension become flocculated in a few seconds to form a soft percolated network of colloidal interactions, which is able to resist stress with an elastic response [30,31]. As time elapses, nucleation of hydration products takes place at contact points between flocculated cement grains on particle surfaces, which turns the local soft colloidal interaction into rigid connections through hydration products [32]. Eventually, the macroscopic stiffening of cementitious mixtures is ascribed to the increase in size and number of rigid interparticle connections.

Regarding AAS mixtures, solid reaction products were found to accumulate on the slag surface in hydroxide media (Fig. 3), which would

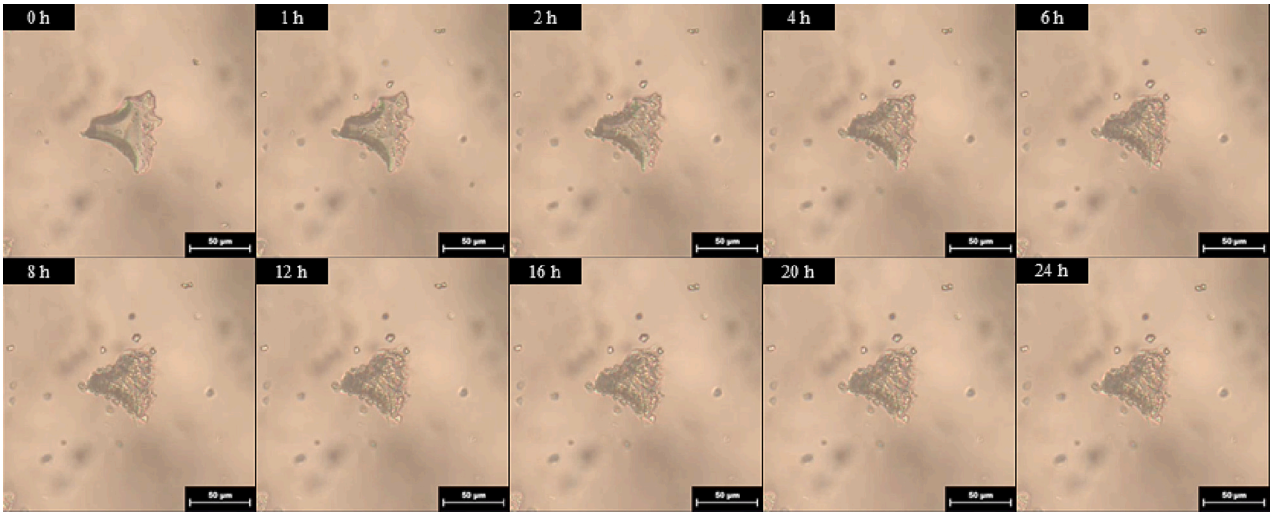

Fig. 3. Microstructure evolution of BFS in sodium hydroxide solution.

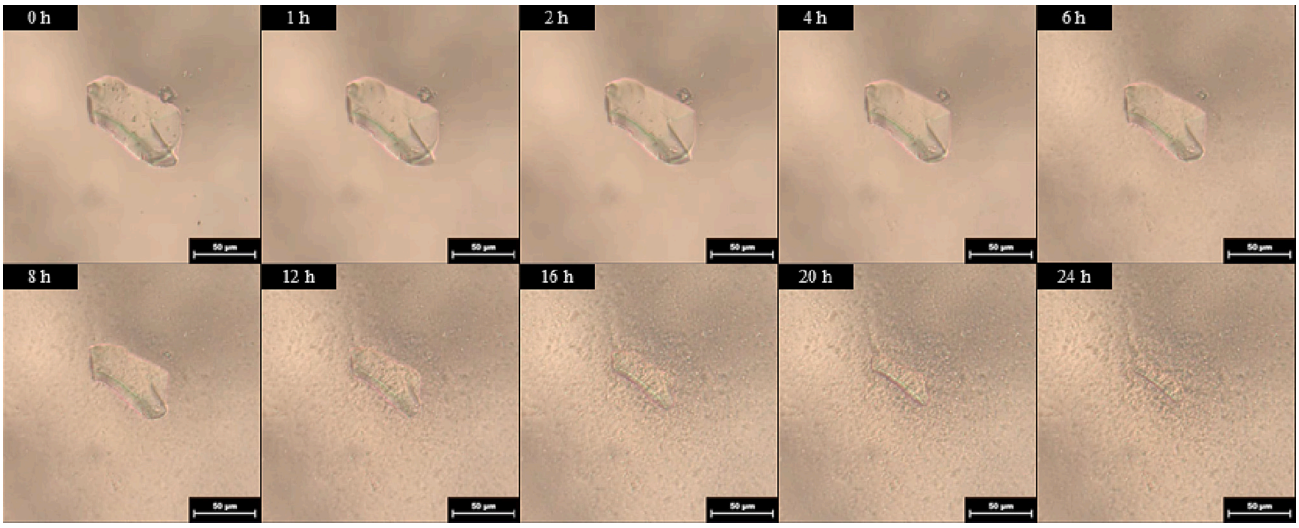

Fig. 4. Microstructure evolution of BFS in sodium silicate solution.

contribute to rigid interparticle connections between flocculated slag particles [16]. However, in the case of mixtures prepared with sodium silicate solutions, negligible colloidal interactions between solid particles at early ages have been reported due to the viscous effect of silicate activators [19,20], which may disperse solid particles to hinder flocculation [16,20]. This is further confirmed by the microstructure evolution observed in Fig. 4, where numerous solid reaction products are nucleated and intensively dispersed in the activator solution. It appears that the microstructure of silicate-activated AAS is incompatible with the flocculated system in PC materials. Thereby, further tests were conducted to interpret the early stiffening process in AAS paste from both physical and chemical perspectives.

3.2. Monitoring on the early-stage reaction process

The well-known Vicat needle penetration and calorimetry test results are presented in Appendix A, and they will be further discussed to interpret the early-stiffening process in Section 3.4.

3.2.1. Ultrasonic pulse velocity (UPV)

Results of UPV evolution are presented in Fig. 5, where two major increments in the velocity could be identified among different AAS mixtures. With the presence of silicate in the activator, very steep growth in the velocity has been observed in the first couple of minutes. Unlike PC materials, where the first UPV growth is attributed to the development of a percolating network through solid hydration products

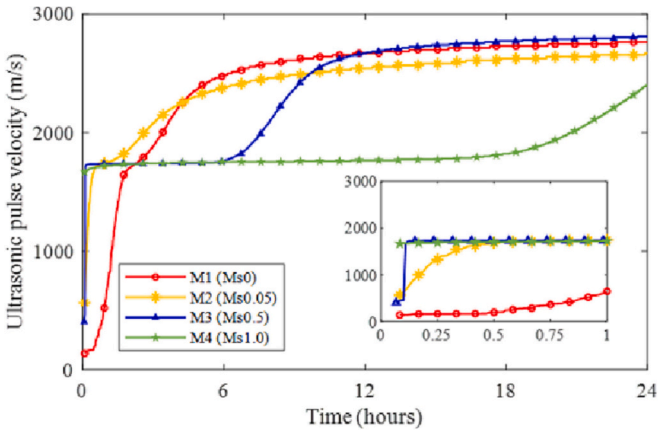

Fig. 5. UPV evolution as a function of time in AAS pastes.

[33], the high initial UPV values detected in silicate-activated AAS pastes might be ascribed to the presence of a well-percolated silicate gel network at early ages [16], which provides an adequate path for ultrasonic waves to propagate at higher speeds. Afterwards, the reactions between cations dissolved from slag particles and silicate species originated from the activators reached an equilibrium [34]. Thereby the UPV evolution reached a plateau and maintained a dormant period for several hours. As presented in Fig. 5 (enlarged view), the initial UPV growth was drastically accelerated with an increase in Ms., and thus the dormant period was advanced. Meanwhile, high Ms on the other hand extended the dormant period. This can be attributed to the limited ion diffusion rate induced by the reaction rim [6,17,35] and primary reaction products [11,34] on the slag surface. Moreover, the initial reactivity might be slowed down as the pH of sodium silicate solutions decreases with higher Ms (as indicated in Table 2), leading to a longer dormant (induction) period. The secondary growth in UPV occurred by the end of the dormant period, which indicates that the silicate species dissolved from slag particles are incorporated to form the reaction products [11,34,36]. Subsequently, the chemical reaction and dissolution reached another equilibrium state, and the UPV development was gradually decelerated to achieve a stable level.

Previous studies suggested that a few conventional monitoring techniques may predict the setting of PC materials, which is revealed by the transition of physical features detected along the hydration process. For instance, Zhang et al. [37] proposed that the initial setting of cement paste typically occurs at the beginning of the acceleration period. Trtnik et al. [38] suggested that the initial setting time of cement paste can be accurately estimated by either the 'first inflection point' or the time when UPV reaches the speed in the water. Similar attempts have been made in this study. Unfortunately, however, no clear relationship has been found. It is indicated that the early-age stiffening of AAS pastes might be following different reaction mechanisms, accompanied by distinctive chemical and physical features.

3.2.2. Structural build-up by SAOS test

The storage modulus (G′) evolution of AAS mixtures is presented in Fig. 6. A rapid structural build-up has been detected in both low and high Ms mixtures, which is consistent with Vicat needle test results. It is noteworthy that M4 exhibited a steeper structural build-up process than M1 and M2 after the initial slow development.

Meanwhile, a distinct structuration history has been observed in intermittent tests, as shown in Fig. 7. The G′ evolution was started with a minimum value in each intermittent time sweep. Due to the earlier strain sweep, the agglomerated particles were dispersed from each other

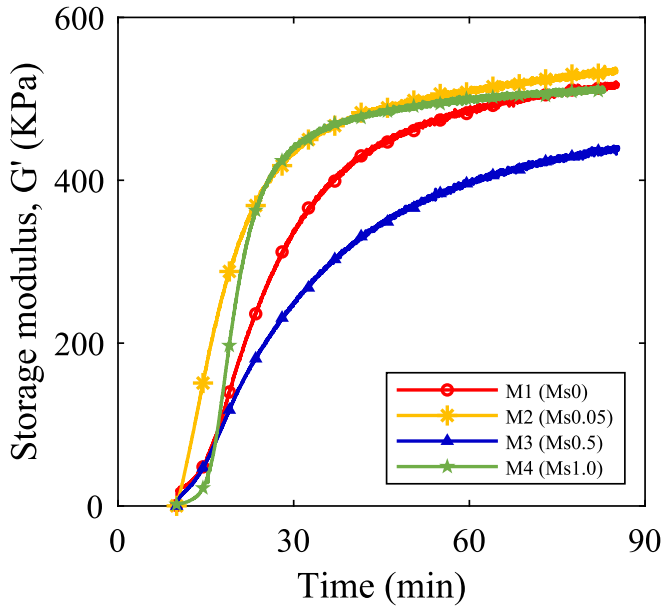

Fig. 6. Evolution of storage modulus as a function of time in AAS pastes (continuous time-sweep).

by the large strain amplitude applied, resulting in a low G′ value [39,40]. Later on, the strain amplitude was switched down within the LVED in the subsequent time sweep. It is indicated that raptured structures were recovered due to the progressive dissolution and activation reaction, leading to the G′ increase with time. A cyclic growth in G′ has been observed in all mixtures, and each strain cycle ended up with a maximum G′ (G'_{max}).

In M1 and M2 (Ms0 and Ms0.05), as indicated by the black curves, G'_{max} continuously increased along with activation time, while in the case of M3 and M4 (Ms0.5 and Ms1.0), a maximum G'_{max} first occurred at early ages, but then declined into lower values as the reaction progressed. Results reveal that the structuration in a silicate-activated AAS system can be partially recovered given a strong enough external shear (e.g., the maximum strain amplitude of 10 % applied in this study), which is in agreement with previous studies that the setting time of a high Ms AAS mixture can be extended by using a longer mixing time [41].

The oscillation stress evolution curves derived from intermittent strain sweep tests are presented in Fig. 8. For each strain sweep, a peak oscillation stress could be identified beyond the initial low strain region. This is followed by a slight reduction in stress values while further increasing the strain amplitude, and finally ended with a secondary stress growth at higher strain levels.

Previous studies have proposed two critical values along with the strain amplitude in PC materials [19,20,32], which originated from the breakage of C-S-H percolating between cement grains and the collapse of colloidal interaction networks, respectively. Similar results have been reported in AAS mixtures [16,20], indicating the first peak observed in Fig. 8 is correlated to C-S-H phases between slag particles. The higher strain amplitude gradually approaches the deforming capacity of colloidal interactions, thereby leading to the secondary increase of stress levels. The strain amplitude at which the first peak stress occurred was defined as ε_1 in this study, and the corresponding oscillation stress was denoted as σ_1. Moreover, previous studies also reported a negligible colloidal interaction, while the viscous effect originated from the interstitial gels is predominant at early ages with a high silicate dosage in both high calcium and low calcium systems [19,20,42]. This can be analogized to the stress-strain curves obtained in M4 at 10 min, where the stress level was much lower with a less prominent peak as compared to later ages.

By varying the Ms in activators, AAS mixtures exhibited different trends in ε_1 and σ_1 evolution over time, as presented in Fig. 9. The initial ε_1 and σ_1 levels achieved in AAS mixtures could be attributed to the early dissolution process, while the further growth in M1 and M2 after 30 min was ascribed to their acceleration stage reactions (Fig. 14(a) and (b)). It is noteworthy that extremely high ε_1 and σ_1 values occurred in M4 between 20 and 30 min. Similarly, Palacios et al. [11] reported an obvious peak of apparent viscosity in a silicate-activated AAS paste under continuous shear conditions. Such observations indicate a rather vigorous reaction associated with the initial dissolution process. Given that, the external shear applied was no longer strong enough to immediately break down the real-time structural build-up, and thus resulted in steep increases in rheological parameters. However, they were later dropped into lower values as the induction period began, and the accumulated structuration was gradually erased by subsequent shear steps.

Regarding M1 and M2, progressive increases in ε_1 and σ_1 have been detected as time elapsed (Fig. 9). Meanwhile, the oscillation stress at 10 % strain amplitude also increased with time (Fig. 8(a) and (b)). As indicated in Fig. 3, the precipitation of reaction products takes place around individual slag particles in hydroxide media. Results obtained here further illustrate that interparticle connections were progressively reinforced due to the local accumulation of reaction products on the slag surface, leading to temporal growth in ε_1 and σ_1.

However, AAS mixtures with a higher Ms (M3 and M4) showed different stress-strain evolution over time. In the case of M4, a significant global increase in stress levels occurred between 10 and 20 min, which can be attributed to the extensive structuration due to the rapid dissolution at this stage. Subsequently, ε_1 gradually declined, accompanied with a reduction in σ_1 at later ages. A possible explanation here would be the majority of early reaction products from the dissolution stage are floating in the pore solution and less contributing to the interconnection between slag particles, as presented in Fig. 4. At this stage, the development of interparticle connections was limited due to the low reaction rate within the induction period, while the existing interparticle interactions were progressively broken down due to the intermittent strain sweep applied, and thereby a declined ε_1 was detected over time. Considering the transparency and fine particles observed in Fig. 4, here the early reaction products could be predominant by oligomeric aluminosilicate species [43,44], which were later synthesized into polymers with higher structural orders through condensation reactions [28,45,46]. This can be supported by the ^{29}Si and ^{27}Al NMR results reported by Puertas et al. [36], that a drastic drop in $Q^1/\sum Q^2$ ratio (Q^1 indicates that the silicate groups are mostly in dimeric units, and $\sum Q^2$ represents silicate groups with higher structure orders [36,47]) in a silicate-activated AAS occurred after 24 h, indicating the formation of longer tetrahedral silicate chains. However, numerous negatively charged oligomers may lead to a significant delay in the polymerization process due to their interparticle repulsions [48], referring to the long induction period observed in high Ms mixtures ([49,50] and M4 in this study shown in Fig. 17). On the other hand, the oscillation stress in the high-strain region (around 10 %) kept increasing over time. It has been illustrated in Fig. 4 that numerous fine granules are nucleated in the pore solution. As a consequence, the volume fraction and surface area in the AAS system are significantly increased. At early ages, the majority of reaction products are dispersed and uniformly distributed in the pore solution, as presented in Fig. 4. However, nucleation fronts continuously develop to approach each other as the reaction proceeds, leading to strong interparticle interactions between fine reaction products. This can be further reflected by the thickening of interstitial gels over time in a silicate-activated AAS [16]. Eventually, rigid connections are developed due to the growth and accumulation of reaction products, which results in macroscopic stiffening of AAS pastes.

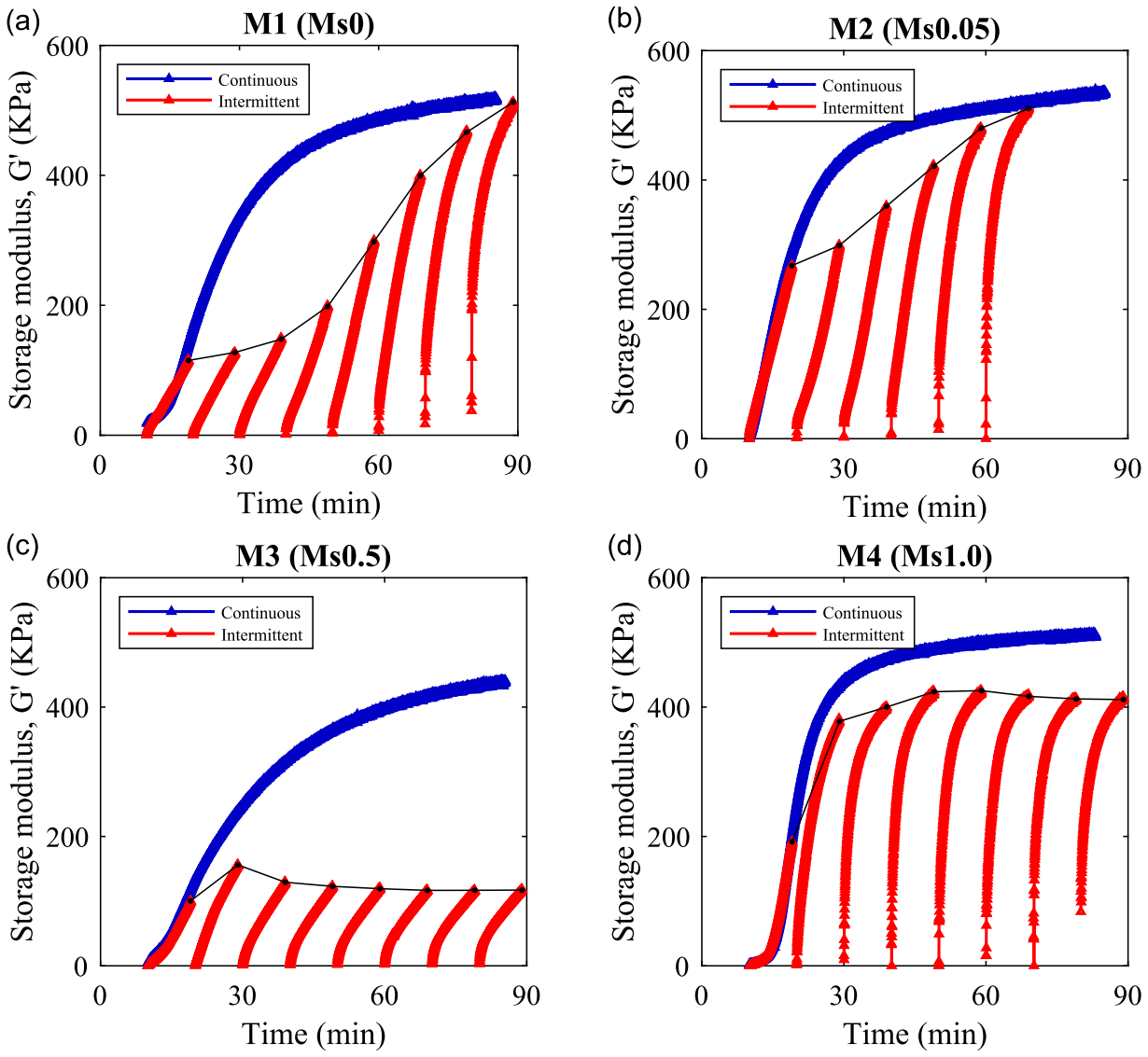

Fig. 7. Evolution of storage modulus as a function of time (a) M1 (Ms0); (b) M2 (Ms0.05); (c) M3 (Ms0.5); (d) M4 (Ms1.0).

3.3. Characterization of hydrating AAS pastes

Characterization of hydrating AAS pastes has been conducted to better understand the reaction mechanism behind the early stiffening process. The pore solution and solid components separated with a 45 μm filtration were collected and analyzed through the methods described in Section 2.3.

3.3.1. Pore solution chemistry

Element concentrations in the pore solution of AAS mixtures are shown in Fig. 10. Due to the nature of activators, Na was detected as the most predominant ion among all mixtures, accompanied with the variation of Si concentrations depending on the Ms applied. The Si concentration in M1 continuously increased since no silicate was predissolved in the activator. It was found that the structural build-up in AAS paste is primarily associated with the reduction of calcium concentration in the pore solution. Ca and Mg divalent cations, as modifiers in aluminosilicate tetrahedral structures [6], have exhibited very similar trends of evolution in different mixtures along the reaction process. A steep increase in their concentrations was observed in the first 10 min, due to the initial dissolution of BFS. The highest content of Ca and Mg in the pore solution was detected in M4 within the dissolution period. It is noticed that the higher the Ms the more Ca and Mg ions are dissolved at this stage, and the maximum Ca concentration of M4 was approximately 180 times higher than that in M1. Results indicate that silicate species in the activator significantly facilitated the dissolution of alkali-earth metals. Eventually, the dissolution and consumption of Ca in AAS mixtures reached an equilibrium, that the concentration was kept nearly constant at later ages. In M4, the reduction of multiple ion concentrations at around 30 min indicates the formation of numerous C-S-H phases, which are present as the intermediate reaction product between the Si originated from the activator and Ca dissolved from slag particles [11], associated with Na and Al incorporations. Regarding the Al content, results show that the Al concentration progressively increased in M1, M2, and M3 over time, while it slightly reduced in M4 after about 30 min, suggesting that the early reaction products in M4 tend to incorporate more Al compared to other mixtures with a lower Ms. Moreover, the pH values in the pore solutions remained at a relatively stable high level until 90 min, with the highest alkalinity being detected in M1.

3.3.2. Solid reaction products

The mass evolution curves of the solid fraction in AAS pastes along the heating process are shown in Fig. 11. The contribution from

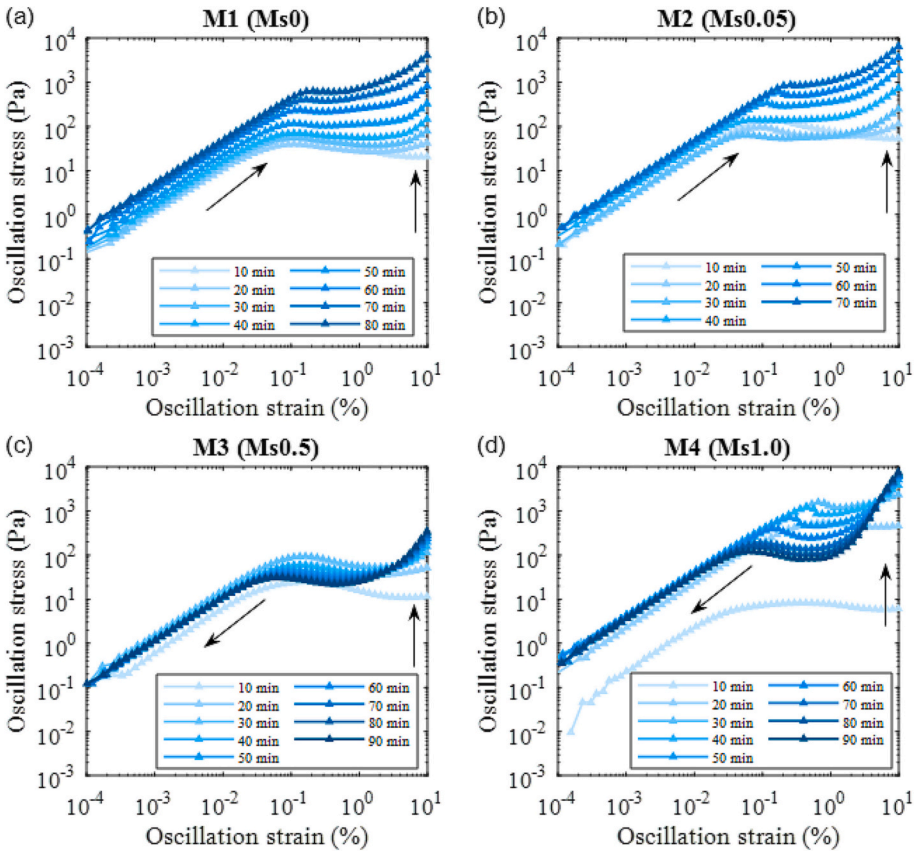

Fig. 8. Evolution of oscillation stress as a function of strain (a) M1 (Ms0); (b) M2 (Ms0.05); (c) M3 (Ms0.5); (d) M4 (Ms1.0).

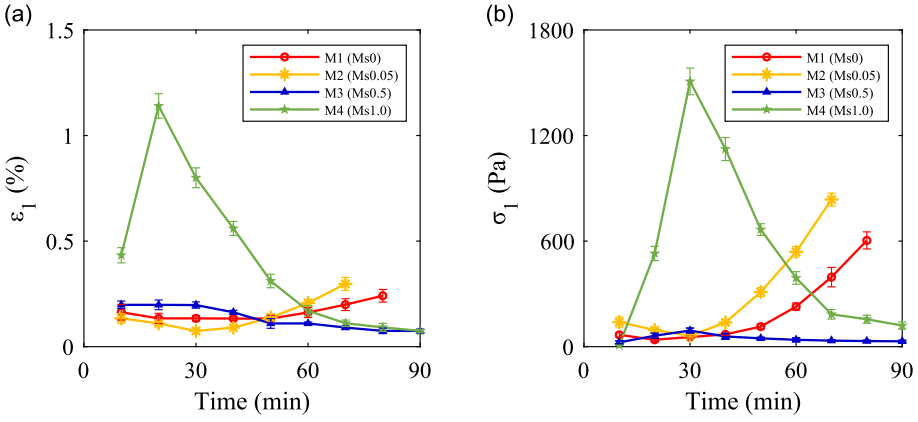

Fig. 9. Evolution of ε_1 and σ_1 detected by intermittent strain-sweep tests (a) ε_1 as a function of time; (b) σ_1 as a function of time (ε_1 is defined as the strain amplitude at which the first peak stress occurred along the strain sweep, and the corresponding oscillation stress was denoted as σ_1).

physically bound water is negligible through solvent exchange and vacuum preparations [51]. Two major peaks were detected in differential thermogravimetry (DTG) curves. The most significant mass loss below 200 °C is attributed to the calcium silicate hydrates (C-S-H phases) [28,52,53], which is also denoted as C-(A)-S-H [54,55] and C-(N)-A-S-H [11,51] gels in AAS systems depending on the incorporation of Al and Na in Si tetrahedrons. Apart from that, the dehydration of hydrotalcite-like (Ht) phases was detected at higher temperatures, represented by the shoulder and sub-peaks observed at around 200 and 400 °C, respectively [56,57]. Further, the mass loss above 500 is ascribed to the decomposition of carbonated phases [58].

As indicated in Fig. 11, early-age hydrates in AAS mixtures are characterized by mass variation up to 500 °C [11]. In M1 and M2, the amount of reaction products progressively increased over time. By contrast, the increase nearly becomes stagnant in M3 and M4 between 60 and 90 min, ascribed to the onset of induction stage reactions. Looking into 30-min DTG curves, M1 was detected with the lowest peak below 200 °C, whereas the mass loss up to 500 °C was intensified with an increase in Ms. Results indicate that higher silicate content resulted in more accumulation of early reaction products, especially C-S-H phases, during the dissolution stage. However, it is noteworthy that M3 with more reaction products exhibited less structural build-up compared to M2 up to 30 min (Fig. 6). This might be attributed to the microstructural configuration that the early reaction products with a smaller grain size are intensively dispersed in high Ms mixtures (Fig. 4), thereby leading to less interparticle connections and flocculation in the system. In addition,

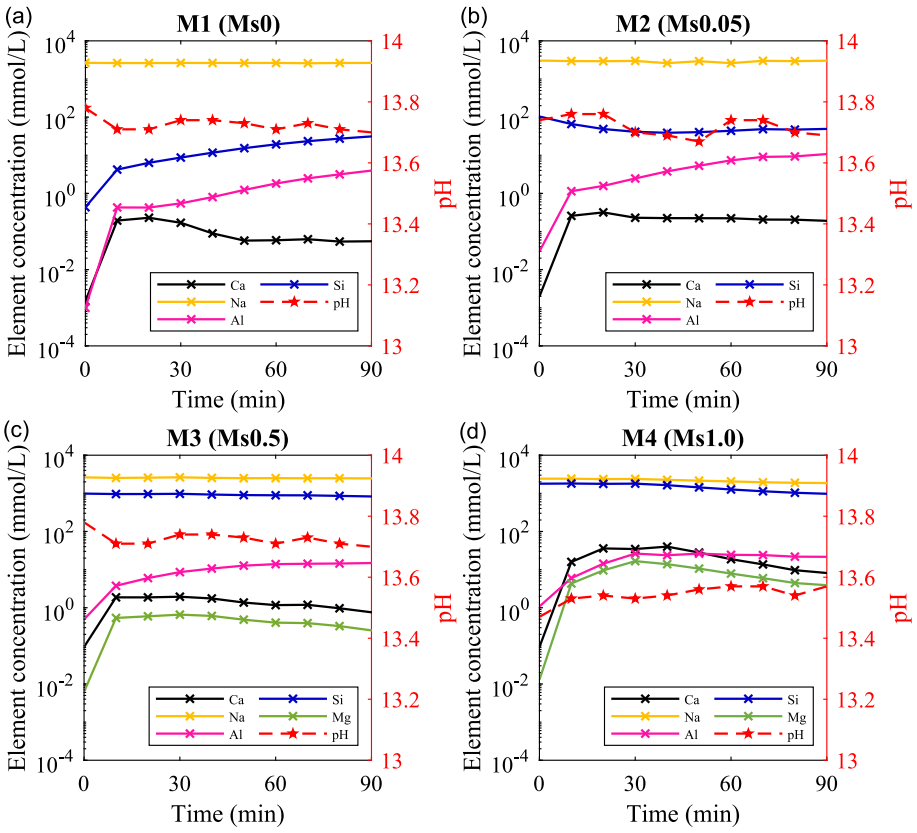

Fig. 10. Element concentration as a function of time in AAS pastes (a) M1 (Ms0); (b) M2 (Ms0.05); (c) M3 (Ms0.5); (d) M4 (Ms1.0). (Note: Mg was detected <0.001 mmol/L in M2 and M4 and not presented.)

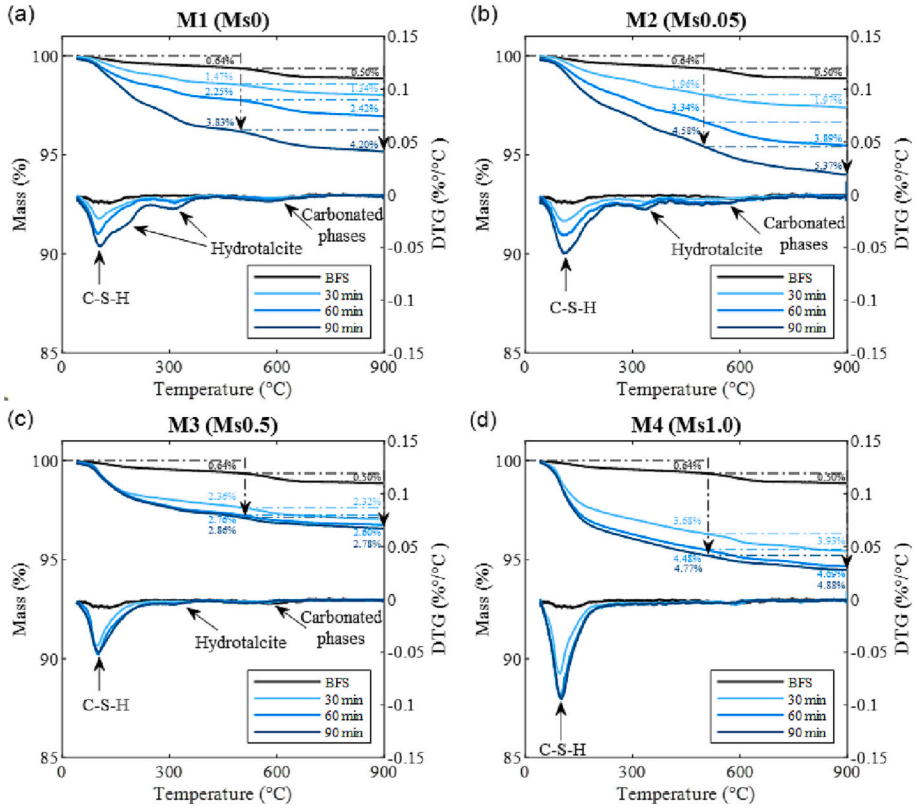

Fig. 11. TG and DTG curves of the solid fraction in hydrating AAS pastes (a) M1 (Ms0); (b) M2 (Ms0.05); (c) M3 (Ms0.5); (d) M4 (Ms1.0).

previous studies further suggested that C-S-H phases formed in hydroxide-activated AAS are more crystallized with less water content [28].

Moreover, obvious Ht peaks have been detected in M1 and M2, whereas Ht phases were significantly reduced with higher Ms. Relevant peaks almost vanished in M4 as presented in Fig. 11(d). Results above indicate that the stiffening of hydroxide-activated AAS mixtures is associated with the development of both C-S-H and Ht phases. With a distinct distribution of reaction products, the accumulation of C-S-H phases is more predominant behind the stiffening of high-Ms AAS mixtures.

As presented in Fig. 12, the development of crystalline phases is very limited in early AAS mixtures. C-S-H and Ht phases, as the typical reaction products in an AAS system [28,34,52–54], were identified with time in XRD patterns. Some minor variations in crystalline phases were observed, which reveals the phase transition along early activation reactions.

C-S-H phases have been detected in all mixtures. A major C-S-H peak could be found at around 29° [28,34], which was progressively developed along with activation reactions. Besides, more crystalline and sodium-rich C-S-H phases (C-S-H (I)) [28] were observed in the hydroxide-activated mixture M1 while comparing with the other AAS mixtures. In M1, it is evident that Ht phases were formed at very early ages (30 min). However, the reflections associated with Ht phases were attenuated with increases in Ms. It appears that diffraction lines associated to Ht phases are not present in M4 samples. The result is consistent with TG analysis, indicating the formation of Ht phases can be inhibited due to the significant lower reaction rate in silicate activators compared to hydroxide activators [34]. Similar results have been reported in previous studies [28,59], and Ht phases were detected in silicate-activated AAS at much later ages. Furthermore, it is noteworthy that XRD patterns of M4 were nearly identical to the anhydrous BFS, which implies a rather limited degree of crystallization in M4 throughout the early stiffening process. This is further confirmed by the fine granules visualized in Fig. 4.

The FTIR spectra of AAS pastes are presented in Fig. 13. As is known, the stretching vibration of T-O (T=Si or Al) bonds are IR active in the range between 800 and 1200 cm^{-1} [60], whereas the broad band observed in this region is attributed to overlaps of amorphous aluminosilicate phases in both precursor and reaction products [61]. The main band located at approximately 950 cm^{-1} is ascribed to the asymmetrical stretching vibration of Si-O-T and Si-O-M (M is alkali/alkali earth metals) bonds, which is recognized as characteristic tetrahedral structures containing C-S-H phases with Al substitutions [62]. In addition, the bands located at lower wavenumbers are assigned to bending vibrations of Si-O-T [54], whereas small peaks at around 1130 and 1160 could be correlated to Si-O-T stretching vibrations [58].

As shown in Fig. 13, the main asymmetric stretching vibration band shifted towards higher wavenumbers as the reaction progressed. Similar results have been reported in AAS at early ages [11,34], which is attributed to the increase in Si/Al ratio in reaction products [63]. In M1 and M2, an explicit peak was detected at around 950 cm^{-1} after 90 min, whereas only a shoulder could be identified in M3 and M4 in the same region. Instead, another peak with lower wavenumbers (at around 900 cm^{-1}) was detected in M3 and M4, suggesting more Al incorporations in reaction products [58]. Walkley et al. [64] proposed that a higher content of soluble silicate in the activator could promote the Al incorporation into aluminosilicate chains. This is in line with the ICP result that Al species are more concentrated in the pore solution of M3 and M4 as compared to M1 and M2 at the same stage. At later ages, Si dissolved from the slag will be incorporated into the gel network, forming Si-rich phases with a higher degree of structural order [36,65]. Further, the band at 688 cm^{-1} in anhydrous slag is associated with the vibration of Al-O bonds [36], and it moved towards lower wavenumbers in AAS

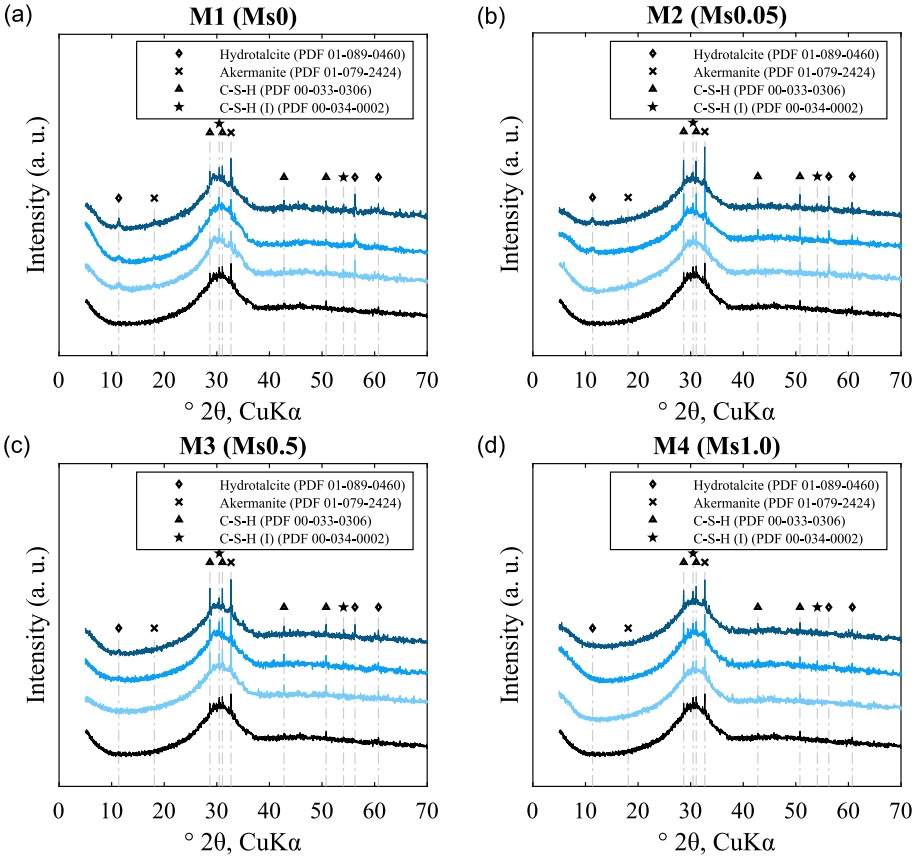

Fig. 12. XRD patterns of the solid fraction in hydrating AAS pastes (a) M1 (Ms0); (b) M2 (Ms0.05); (c) M3 (Ms0.5); (d) M4 (Ms1.0).

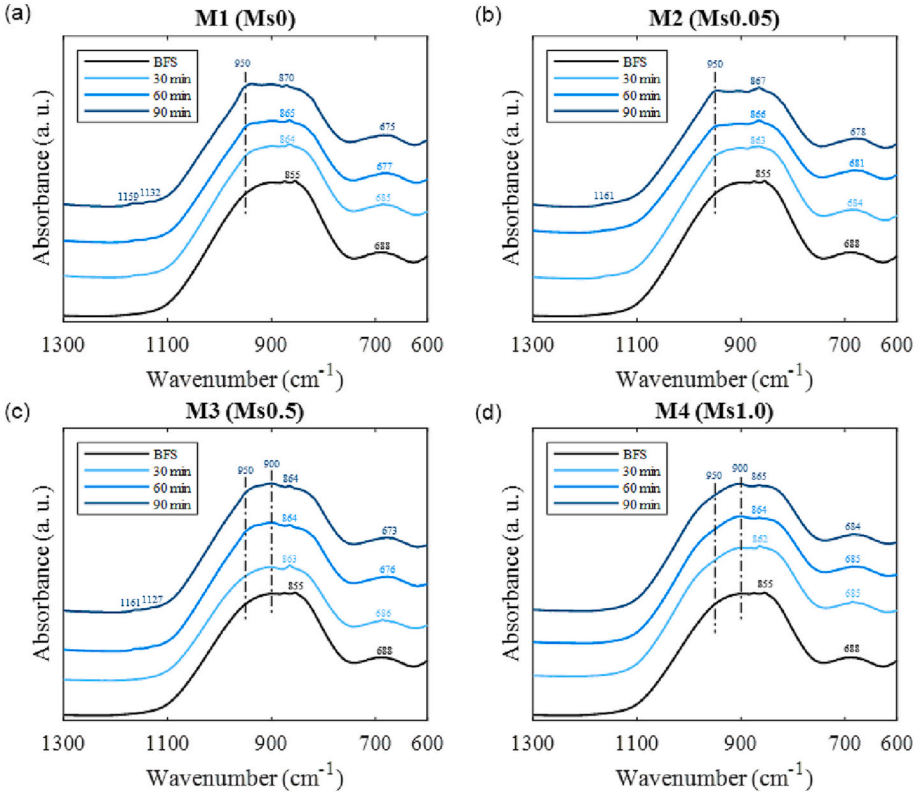

Fig. 13. FTIR spectra of the solid fraction in hydrating AAS pastes (a) M1 (Ms0); (b) M2 (Ms0.05); (c) M3 (Ms0.5); (d) M4 (Ms1.0).

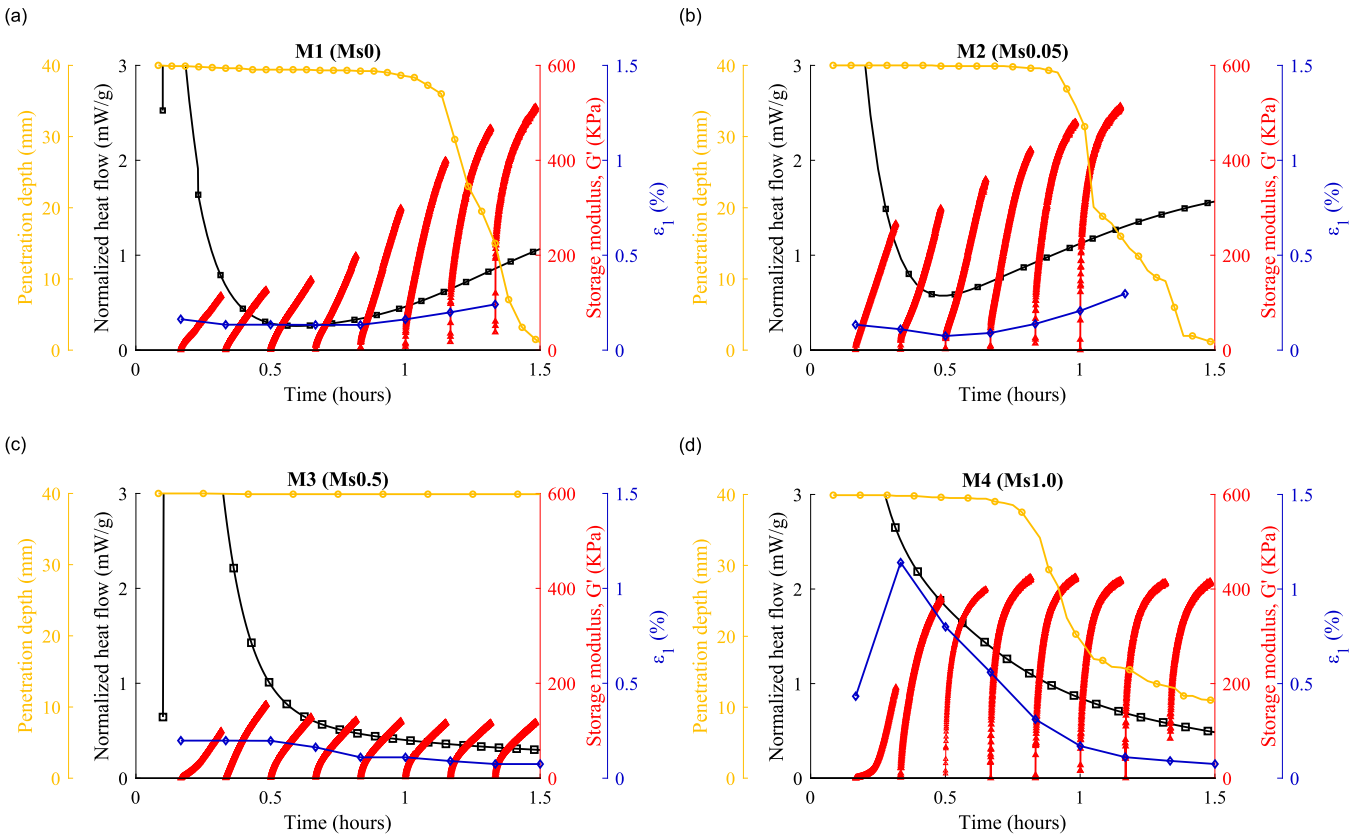

Fig. 14. Monitoring on the early-age stiffening process of AAS pastes (a) M1 (Ms0); (b) M2 (Ms0.05); (c) M3 (Ms0.5); (d) M4 (Ms1.0).

pastes. The small band located at 855 cm^{-1} originates from symmetric stretching vibrations of Si-O in BFS [62], which became less intensive with time elapsed due to the continuous dissolution.

3.4. Interpretation of the early stiffening process

Monitoring results of early-age (0–1.5 h) AAS pastes are summarized in Fig. 14. It is indicated that there is a competition between different mechanisms behind the stiffening of AAS mixtures, depending on the silicate modulus in the activator. It is interesting to notice that the G'_{max} evolution is in good correlation with the exothermic behaviors (Fig. 14). The G'_{max} development can be further divided into two stages, corresponding to explicit exothermic processes (i.e. the dissolution peak and acceleration peak, as shown in the enlarged view in Fig. 17). To be specific, in M3 and M4, the maximum G'_{max} occurred at around 30 and 60 min, which is in parallel with the end of their dissolution peaks, respectively. In the meantime, a broader dissolution peak accompanied with a higher G'_{max} was detected in M4, where more silicate content (Ms1.0) was applied. It can be inferred that massive cations were dissolved from the slag particles at this stage (as shown in Fig. 10) to interact with the silicate species present in the activator solution [11,12], and thus contributed to the initial growth in G'_{max}. Afterwards, the reaction came into the induction period, associated with a lower heat flow. At this stage, the structuration in AAS maintained limited and thereby can be recovered by external shear, as indicated by the reduction in G'_{max} in Fig. 7(c) and (d). Regarding M1 and M2 (Ms0 and Ms0.05), similar G'_{max} evolution due to the early dissolution could be expected in the first couple of minutes. In both M1 and M2, the reaction progressed very fast and no obvious induction period was identified. The continuous G'_{max} increase at later ages observed in M1 and M2 is correlated to their early acceleration stage reactions. It was found that M2 with a more intensive heat flow from 30 to 60 min achieved higher G'_{max} values as compared to M1 during the same period. Therefore, it is indicated that the early structural build-up in AAS mixtures can be correlated to the dissolution and acceleration stage reactions.

In high-Ms conditions, the early structuration was found in parallel with the dissolution peak detected by calorimetry. Afterwards, the induction period occurred, associated with a relatively low reaction rate and decrease in G'_{max} measured with intermittent SAOS test. C-S-H phases were detected as the primary reaction product, with more Al incorporations in the network. Meanwhile, a gradual reduction in ε_1 was observed, indicating the development of interparticle connections was limited at this stage, which was gradually broken down by subsequent shear steps. This is consistent with the microstructural features that numerous fine granules have been observed to nucleate, which were less connected to each other and intensively dispersed in the activator solution.

However, low-Ms mixtures exhibited a continuous growth in G'_{max}, even though intermittent strain sweeps were applied. This is ascribed to the early onset of acceleration stage reactions. Both C-S-H and Ht were identified as the major reaction products at early ages, leading to the formation of more crystalline phases. Moreover, the increase in ε_1 over time also reveals the progressive strengthening of interparticle connections through reaction products. This is supported by the microscopy that the reaction products are closely attached to the slag surface to form a flocculated system.

Results reveal that the stiffening of AAS mixtures can be attributed to different mechanisms. In a sodium hydroxide-activated AAS, the stiffening process is similar to PC materials. Reaction products are accumulated on the slag surface at contact points (Fig. 15(a)), leading to stronger interparticle connections and the stiffening of AAS mixtures. With the increase of Ms., the viscous effect of activators becomes predominant in the system. Since the silicate content is present as interstitial gels to disperse solid grains [16], colloidal interactions between precursor particles become negligible [20], which is incompatible with the flocculated system in a hydrating PC material. On the other hand, numerous fine granules of early reaction products are nucleated in activator solutions. Accordingly, the solid fraction and surface area in the system are significantly increased. As the reaction proceeds, dispersed reaction product particles continuously develop to approach each other (Fig. 15(b)), which might intensify the interparticle interactions and macroscopically results in the stiffening of AAS. Massive nucleation sites distributed in the pore solution also result in a more rapid global structural development, thereby M4 showed a steeper structuration than M1 and M2 (Fig. 6), where the reaction products preferably precipitate at contact points on the slag surface. It is indicated that the early structural build-up of silicate-activated AAS mixtures could be attributed to the accumulation of intermediate reaction

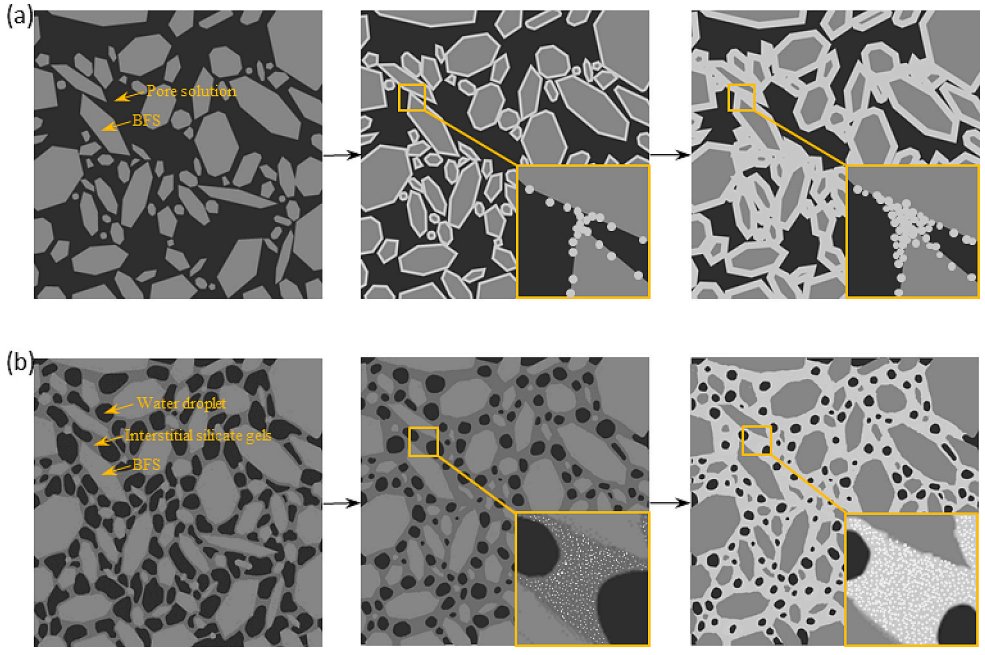

Fig. 15. Schematic sketch on the stiffening process of AAS pastes (a) hydroxide-activated AAS paste; (b) silicate-activated AAS paste (reaction products are represented with grey dots, the variation in grain sizes referring to the microstructure observed in Figs. 3 and 4).

products and thickening of interstitial gels [11,16]. Given a high silicate dosage, the initial setting might have fallen into the dissolution stage. However, the elasticity developed in high-Ms AAS mixtures upon setting seldom contributes to the hardening and strength development like PC materials, which is associated with acceleration stage reactions. High-Ms AAS mixtures in turn may exhibit very limited first-day strength development [15,17], affecting subsequent operations in practical applications (e.g. demolding, upper formwork installation, etc.). Early reaction products in high-Ms AAS are interconnected at later ages through poly-condensation reactions [28,36], which indicates that the real strength development begins only if the long induction stage is terminated. Finally, the present results suggest that a moderate silicate dosage (as per the Ms0.5 mixture in this study) ensures both a good initial flow and a mild dissolution process. In that case, the fluidity of AAS can be maintained until the end of the induction stage.

4. Conclusions

In this research, a comprehensive investigation has been conducted to assess the early stiffening process of alkali-activated slag (AAS) pastes with various silicate modulus (Ms). Multiple approaches were employed to monitor the activation reaction. Besides, separate models were proposed to interpret the early stiffening process. The following conclusions could be drawn based on the results present:

- It was found that the incorporation of silicate content in the activator has resulted in significant impacts on the evolution of microstructural features and reaction products in AAS. A good correlation was observed between the structural build-up and exothermic reactions in AAS.
- In hydroxide-activated AAS, the precipitation of reaction products was found to take place around individual slag grains, where hydrotalcite and C-S-H phases were characterized as major reaction products at early ages.
- Results of the time-sweep test indicate that the interparticle connections were progressively strengthened along the reaction process. The stiffening of hydroxide-activated AAS is similar to that in PC materials, which is attributed to the formation of a well-percolated network through solid reaction products.
- With the increase of Ms., nucleation sites become available in the pore solution. Early reaction products with much smaller particle sizes have been observed, which were intensively dispersed in the activator solution, leading to a less flocculated system.
- Compared to hydroxide-activated AAS, the development of interparticle connections in silicate-activated AAS mixtures was limited at early ages. In addition, early reaction products were detected with less crystalline phases and higher Al incorporations.
- The stiffening of high-Ms AAS mixtures could be ascribed to the accumulation of early reaction products and the thickening of interstitial gels. As the reaction progresses, the volume fraction and surface area are significantly improved in the system. Fine particles of reaction products continuously develop to approach each other, which may intensify the interparticle interactions and result in the macroscope stiffening of silicate-activated AAS.

Supplementary data to this article can be found online at https://doi.org/10.1016/j.cemconres.2023.107118.

CRediT authorship contribution statement

Yubo Sun: Conceptualization, Methodology, Investigation, Writing – original draft. **Luiz Miranda de Lima:** Methodology, Investigation, Writing – review & editing. **Laura Rossi:** Methodology, Investigation, Writing – review & editing. **Dengwu Jiao:** Methodology, Investigation, Writing – review & editing. **Zhenming Li:** Methodology, Writing – review & editing. **Guang Ye:** Supervision, Writing – review & editing. **Geert De Schutter:** Funding acquisition, Supervision, Writing – review & editing.

Declaration of competing interest

The authors declared that they have no conflicts of interest in this work. The authors declare that they do not have any commercial or associative interest that represents a conflict of interest in connection with the work submitted.

Data availability

Data will be made available on request.

Acknowledgments

This paper presents the research results from the DuRSAAM project. The financial support from the European Union's Horizon 2020 - Research and Innovation Framework Programme (ETN DuRSAAM – H2020-MSCA-ITN-2018-813596) is gratefully acknowledged.

Appendix A

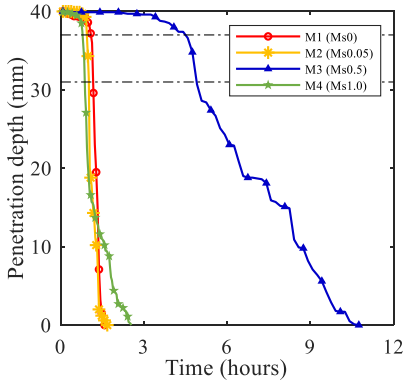

Fig. 16. Vicat needle penetration depth as a function of time in AAS pastes.

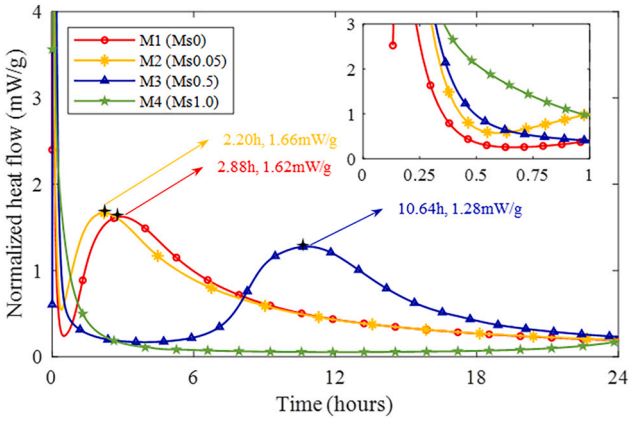

Fig. 17. Heat flow evolution as a function of time in AAS pastes.

References

[1] M.C.G. Juenger, F. Winnefeld, J.L. Provis, J.H. Ideker, Advances in alternative cementitious binders, Cem. Concr. Res. 41 (2011) 1232–1243, https://doi.org/10.1016/j.cemconres.2010.11.012.

[2] L. Coppola, T. Bellezze, A. Belli, M.C. Bignozzi, F. Bolzoni, A. Brenna, M. Cabrini, S. Candamano, M. Cappai, D. Caputo, Binders alternative to Portland cement and waste management for sustainable construction—Part 1, J. Appl. Biomater. Funct. Mater. 16 (2018) 186–202.

[3] J.L. Provis, J.S.J.Van Deventer, Alkali activated materials: state-of-the-art report, in: RILEM TC 224-AAM, Springer Science & Business Media, 2013.

[4] M. Fawer, M. Concannon, W. Rieber, Life cycle inventories for the production of sodium silicates, Int. J. Life Cycle Assess. 4 (1999) 207–212.

[5] L.K. Turner, F.G. Collins, Carbon dioxide equivalent (CO2-e) emissions: a comparison between geopolymer and OPC cement concrete, Constr. Build. Mater. 43 (2013) 125–130, https://doi.org/10.1016/j.conbuildmat.2013.01.023.

[6] P. Duxson, J.L. Provis, Designing precursors for geopolymer cements, J. Am. Ceram. Soc. 91 (2008) 3864–3869, https://doi.org/10.1111/j.1551-2916.2008.02787.x.

[7] S.R. Gislason, E.H. Oelkers, Mechanism, rates, and consequences of basaltic glass dissolution: II. An experimental study of the dissolution rates of basaltic glass as a function of pH and temperature, Geochim. Cosmochim. Acta 67 (2003) 3817–3832.

[8] A. Fernández-Jiménez, J.G. Palomo, F. Puertas, Alkali-activated slag mortars: mechanical strength behaviour, Cem. Concr. Res. 29 (1999) 1313–1321, https://doi.org/10.1016/S0008-8846(99)00154-4.

[9] M. Albitar, M.S.M. Ali, P. Visintin, M. Drechsler, Durability evaluation of geopolymer and conventional concretes, Constr. Build. Mater. 136 (2017) 374–385, https://doi.org/10.1016/j.conbuildmat.2017.01.056.

[10] T.A. Aiken, W. Sha, J. Kwasny, M.N. Soutsos, Cement and concrete research resistance of geopolymer and Portland cement based systems to silage ef fl uent attack, Cem. Concr. Res. 92 (2017) 56–65, https://doi.org/10.1016/j.cemconres.2016.11.015.

[11] M. Palacios, S. Gismera, M.M. Alonso, J.B. Espinose, D. Lacaillerie, B. Lothenbach, A. Favier, C. Brumaud, F. Puertas, Cement and concrete research early reactivity of sodium silicate-activated slag pastes and its impact on rheological properties, Cem. Concr. Res. 140 (2021), 106302, https://doi.org/10.1016/j.cemconres.2020.106302.

[12] M. Palacios, P.F.G. Banfill, F. Puertas, Rheology and setting of alkali-activated slag pastes and mortars: effect of organic admixture, ACI Mater. J. 105 (2008) 140.

[13] C. Qing-Hua, S.L. Sarkar, A study of rheological and mechanical properties of mixed alkali activated slag pastes, Adv. Cem. Based Mater. 1 (1994) 178–184, https://doi.org/10.1016/1065-7355(94)90009-4.

[14] E. Douglas, A. Bilodeau, V.M. Malhotra, Properties and durability of alkali-activated slag concrete, Mater. J. 89 (1992) 509–516.

[15] D. Ravikumar, N. Neithalath, Effects of activator characteristics on the reaction product formation in slag binders activated using alkali silicate powder and NaOH, Cem. Concr. Compos. 34 (2012) 809–818, https://doi.org/10.1016/j.cemconcomp.2012.03.006.

[16] Y. Sun, S. Zhang, A.V. Rahul, Y. Tao, F. Van Bockstaele, K. Dewettinck, G. Ye, G. De Schutter, Rheology of alkali-activated slag pastes: new insight from microstructural investigations by cryo-SEM, Cem. Concr. Res. 157 (2022), 106806, https://doi.org/10.1016/j.cemconres.2022.106806.

[17] B.S. Gebregziabiher, R. Thomas, S. Peethamparan, Very early-age reaction kinetics and microstructural development in alkali-activated slag, Cem. Concr. Compos. 55 (2015) 91–102, https://doi.org/10.1016/j.cemconcomp.2014.09.001.

[18] F. Puertas, C. Varga, M.M. Alonso, Rheology of alkali-activated slag pastes. Effect of the nature and concentration of the activating solution, Cem. Concr. Compos. 53 (2014) 279–288, https://doi.org/10.1016/j.cemconcomp.2014.07.012.

[19] A. Favier, J. Hot, G. Habert, N. Roussel, J.B. D'Espinose De Lacaillerie, Flow properties of MK-based geopolymer pastes. A comparative study with standard Portland cement pastes, Soft Matter 10 (2014) 1134–1141, https://doi.org/10.1039/c3sm51889b.

[20] M.F. Alnahhal, T. Kim, A. Hajimohammadi, Distinctive rheological and temporal viscoelastic behaviour of alkali-activated fly ash/slag pastes: a comparative study with cement paste, Cem. Concr. Res. 144 (2021), 106441, https://doi.org/10.1016/j.cemconres.2021.106441.

[21] A. Favier, G. Habert, J.B. D'Espinose De Lacaillerie, N. Roussel, Mechanical properties and compositional heterogeneities of fresh geopolymer pastes, Cem. Concr. Res. 48 (2013) 9–16, https://doi.org/10.1016/j.cemconres.2013.02.001.

[22] P. Romero, N. Garg, Evolution of kaolinite morphology upon exfoliation and dissolution: evidence for nanoscale layer thinning in metakaolin, Appl. Clay Sci. 222 (2022), 106486, https://doi.org/10.1016/j.clay.2022.106486.

[23] L. Wadsö, Operational issues in isothermal calorimetry, Cem. Concr. Res. 40 (2010) 1129–1137.

[24] H.W. Reinhardt, C.U. Grosse, Continuous monitoring of setting and hardening of mortar and concrete, Constr. Build. Mater. 18 (2004) 145–154, https://doi.org/10.1016/j.conbuildmat.2003.10.002.

[25] Q. Yuan, D. Zhou, K.H. Khayat, D. Feys, C. Shi, On the measurement of evolution of structural build-up of cement paste with time by static yield stress test vs. Small amplitude oscillatory shear test, Cem. Concr. Res. 99 (2017) 183–189.

[26] A. Poulesquen, F. Frizon, D. Lambertin, Rheological behavior of alkali-activated metakaolin during geopolymerization, J. Non-Cryst. Solids 357 (2011) 3565–3571, https://doi.org/10.1016/j.jnoncrysol.2011.07.013.

[27] Y. Qian, K. Lesage, K. El Cheikh, G. De Schutter, Effect of polycarboxylate ether superplasticizer (PCE) on dynamic yield stress, thixotropy and flocculation state of fresh cement pastes in consideration of the critical micelle concentration (CMC), Cem. Concr. Res. 107 (2018) 75–84.

[28] M. Ben Haha, G. Le Saout, F. Winnefeld, B. Lothenbach, Influence of activator type on hydration kinetics, hydrate assemblage and microstructural development of alkali activated blast-furnace slags, Cem. Concr. Res. 41 (2011) 301–310, https://doi.org/10.1016/j.cemconres.2010.11.016.

[29] D. Jiao, R. De Schryver, C. Shi, G. De Schutter, Thixotropic structural build-up of cement-based materials: a state-of-the-art review, Cem. Concr. Compos. 122 (2021), 104152.

[30] J.E. Wallevik, Rheological properties of cement paste: thixotropic behavior and structural breakdown, Cem. Concr. Res. 39 (2009) 14–29, https://doi.org/10.1016/j.cemconres.2008.10.001.

[31] N. Roussel, A thixotropy model for fresh fluid concretes: theory, validation and applications, Cem. Concr. Res. 36 (2006) 1797–1806, https://doi.org/10.1016/j.cemconres.2006.05.025.

[32] N. Roussel, G. Ovarlez, S. Garrault, C. Brumaud, The origins of thixotropy of fresh cement pastes, Cem. Concr. Res. 42 (2012) 148–157, https://doi.org/10.1016/j.cemconres.2011.09.004.

[33] K.M. Lee, H.K. Lee, S.H. Lee, G.Y. Kim, Autogenous shrinkage of concrete containing granulated blast-furnace slag, Cem. Concr. Res. 36 (2006) 1279–1285.

[34] R. Cao, S. Zhang, N. Banthia, Y. Zhang, Z. Zhang, Interpreting the early-age reaction process of alkali-activated slag by using combined embedded ultrasonic measurement, thermal analysis, XRD, FTIR and SEM, Compos. Part B Eng. 186 (2020), 107840, https://doi.org/10.1016/j.compositesb.2020.107840.

[35] Y. Zuo, G. Ye, Preliminary interpretation of the induction period in hydration of sodium hydroxide/silicate activated slag, Materials (Basel) 13 (2020) 1–19, https://doi.org/10.3390/ma13214796.

[36] F. Puertas, A. Fernández-Jiménez, M.T. Blanco-Varela, Pore solution in alkali-activated slag cement pastes. Relation to the composition and structure of calcium silicate hydrate, Cem. Concr. Res. 34 (2004) 139–148, https://doi.org/10.1016/S0008-8846(03)00254-0.

[37] M. Zhang, K. Sisomphon, T.S. Ng, D.J. Sun, Effect of superplasticizers on workability retention and initial setting time of cement pastes, Constr. Build. Mater. 24 (2010) 1700–1707, https://doi.org/10.1016/j.conbuildmat.2010.02.021.
[38] G. Trtnik, G. Turk, F. Kavčič, V.B. Bosiljkov, Possibilities of using the ultrasonic wave transmission method to estimate initial setting time of cement paste, Cem. Concr. Res. 38 (2008) 1336–1342, https://doi.org/10.1016/j.cemconres.2008.08.003.
[39] L. Nachbaur, J.C. Mutin, A. Nonat, L. Choplin, Dynamic mode rheology of cement and tricalcium silicate pastes from mixing to setting, Cem. Concr. Res. 31 (2001) 183–192.
[40] A.M. Betioli, P.J.P. Gleize, D.A. Silva, V.M. John, R.G. Pileggi, Effect of HMEC on the consolidation of cement pastes: isothermal calorimetry versus oscillatory rheometry, Cem. Concr. Res. 39 (2009) 440–445.
[41] M. Palacios, F. Puertas, Effectiveness of mixing time on hardened properties of waterglass-activated slag pastes and mortars, ACI Mater. J. 108 (2011) 73.
[42] X. Dai, S. Aydin, M. Yücel, G. De Schutter, Rheology and structural build-up of sodium silicate- and sodium hydroxide-activated GGBFS mixtures, Cem. Concr. Compos. 131 (2022), 104570, https://doi.org/10.1016/j.cemconcomp.2022.104570.
[43] K. Gong, Y. Cheng, L.L. Daemen, C.E. White, In situ quasi-elastic neutron scattering study on the water dynamics and reaction mechanisms in alkali-activated slags, Phys. Chem. Chem. Phys. 21 (2019) 10277–10292, https://doi.org/10.1039/c9cp00889f.
[44] J.L. Provis, J.S.J. van Deventer, Geopolymerisation kinetics. 2. Reaction kinetic modelling, Chem. Eng. Sci. 62 (2007) 2318–2329, https://doi.org/10.1016/j.ces.2007.01.028.
[45] Y.-S. Wang, Y. Alrefaei, J.-G. Dai, Silico-aluminophosphate and alkali-aluminosilicate geopolymers: a comparative review, Front. Mater. 6 (2019) 106.
[46] J. Davidovits, Properties of geopolymer cements, in: First Int. Conf. Alkaline Cem. Concr, Kiev State Technical University Kiev, Ukraine, 1994, pp. 131–149.
[47] N.J. Clayden, S. Esposito, A. Aronne, P. Pernice, Solid state 27Al NMR and FTIR study of lanthanum aluminosilicate glasses, J. Non-Cryst. Solids 258 (1999) 11–19.
[48] X. Dai, S. Aydın, M. Yücel, K. Lesage, G. De Schutter, Cement and concrete research effects of activator properties and GGBFS / FA ratio on the structural build-up and rheology of AAC, Cem. Concr. Res. 138 (2020), 106253, https://doi.org/10.1016/j.cemconres.2020.106253.
[49] C. Shi, R.L. Day, A calorimetric study of early hydration of alkali-slag cements, Cem. Concr. Res. 25 (1995) 1333–1346.
[50] B.S. Gebregziabiher, R.J. Thomas, S. Peethamparan, Temperature and activator effect on early-age reaction kinetics of alkali-activated slag binders, Constr. Build. Mater. 113 (2016) 783–793, https://doi.org/10.1016/j.conbuildmat.2016.03.098.
[51] S. Zhang, Z. Li, B. Ghiassi, S. Yin, G. Ye, Fracture properties and microstructure formation of hardened alkali-activated slag/fly ash pastes, Cem. Concr. Res. 144 (2021), 106447.
[52] M. Ben Haha, B. Lothenbach, G.L. Le Saout, F. Winnefeld, Influence of slag chemistry on the hydration of alkali-activated blast-furnace slag—Part I: effect of MgO, Cem. Concr. Res. 41 (2011) 955–963.
[53] M. Ben Haha, B. Lothenbach, G. Le Saout, F. Winnefeld, Influence of slag chemistry on the hydration of alkali-activated blast-furnace slag - part II: effect of Al2O3, Cem. Concr. Res. 42 (2012) 74–83, https://doi.org/10.1016/j.cemconres.2011.08.005.
[54] I. Garcia-Lodeiro, A. Palomo, A. Fernández-Jiménez, D.E. MacPhee, Compatibility studies between N-A-S-H and C-A-S-H gels. Study in the ternary diagram Na2O-CaO-Al2O3-SiO 2–H2O, Cem. Concr. Res. 41 (2011) 923–931, https://doi.org/10.1016/j.cemconres.2011.05.006.
[55] E. Kapeluszna, Ł. Kotwica, A. Różycka, Ł. Gołek, Incorporation of Al in CASH gels with various Ca/Si and Al/Si ratio: microstructural and structural characteristics with DTA/TG, XRD, FTIR and TEM analysis, Constr. Build. Mater. 155 (2017) 643–653.
[56] E. Kanezaki, Thermal behavior of the hydrotalcite-like layered structure of mg and Al-layered double hydroxides with interlayer carbonate by means of in situ powder HTXRD and DTA/TG, Solid State Ionics 106 (1998) 279–284.
[57] K. Rozov, U. Berner, C. Taviot-Gueho, F. Leroux, G. Renaudin, D. Kulik, L. W. Diamond, Synthesis and characterization of the LDH hydrotalcite–pyroaurite solid-solution series, Cem. Concr. Res. 40 (2010) 1248–1254.
[58] S. Zhang, A. Keulen, K. Arbi, G. Ye, Waste glass as partial mineral precursor in alkali-activated slag/fly ash system, Cem. Concr. Res. 102 (2017) 29–40, https://doi.org/10.1016/j.cemconres.2017.08.012.
[59] S.-D. Wang, K.L. Scrivener, Hydration products of alkali activated slag cement, Cem. Concr. Res. 25 (1995) 561–571.
[60] M. Criado, A. Fernández-Jiménez, A. Palomo, Alkali activation of fly ash: effect of the SiO2/Na2O ratio. Part I: FTIR study, Microporous Mesoporous Mater. 106 (2007) 180–191, https://doi.org/10.1016/j.micromeso.2007.02.055.
[61] D. Dimas, I. Giannopoulou, D. Panias, Polymerization in sodium silicate solutions: a fundamental process in geopolymerization technology, J. Mater. Sci. 44 (2009) 3719–3730, https://doi.org/10.1007/s10853-009-3497-5.
[62] Z. Li, T. Lu, X. Liang, H. Dong, G. Ye, Mechanisms of autogenous shrinkage of alkali-activated slag and fly ash pastes, Cem. Concr. Res. 135 (2020), 106107, https://doi.org/10.1016/j.cemconres.2020.106107.
[63] Z. Zhang, Y. Zhu, H. Zhu, Y. Zhang, J.L. Provis, H. Wang, Effect of drying procedures on pore structure and phase evolution of alkali-activated cements, Cem. Concr. Compos. 96 (2019) 194–203, https://doi.org/10.1016/j.cemconcomp.2018.12.003.
[64] B. Walkley, X. Ke, J.L. Provis, S.A. Bernal, Activator anion influences the nanostructure of alkali-activated slag cements, J. Phys. Chem. C 125 (2021) 20727–20739, https://doi.org/10.1021/acs.jpcc.1c07328.
[65] P. Duxson, A. Fernández-Jiménez, J.L. Provis, G.C. Lukey, A. Palomo, J.S.J. Van Deventer, Geopolymer technology: the current state of the art, J. Mater. Sci. 42 (2007) 2917–2933, https://doi.org/10.1007/s10853-006-0637-z.